crystals

MDPI

Article

Microstructural Characteristics and Mechanical Properties of an Additively Manufactured Nickel-Based Superalloy

Ke Ma [1] and Jinhai Wang [2,*]

[1] School of Furniture and Art Design, Central South University of Forestry and Technology, Changsha 410018, China
[2] Guangdong Hanbang 3D Technology Co., Ltd., Zhongshan 528427, China
* Correspondence: wangjh@hb3dp.com

Abstract: The nickel-based superalloys processed by additive manufacturing are very promising structural materials in aircraft engines as high-pressure turbine discs. In this work, a nickel-based superalloy with good mechanical performance and few defects was manufactured by optimized selective laser melting (SLM) processing. We then investigated the influences of post heat treatments on its microstructural characteristics and mechanical performance. The results indicated that a fine grain size with uniform grain orientation was presented in the as-printed nickel-based superalloy sample. After heat treatments, the grains were slightly grown and grain orientation was also changed. Under transmission electron microscopy, fine subgrains with an approximate size of 0.5 μm were found in the as-printed sample which accompanied massive dislocations and discontinuous Laves phases. After the post heat treatments, fine subgrains and less dislocations were retained. On the other hand, massive γ' and γ'' precipitates with an orientation relationship of $(001)[100]\gamma'//(100)[001]\gamma$ or $(001)[100]\gamma''//(100)[001]\gamma$ were formed. As a result, the yield stress and tensile strength increased to 1362 and 1410 MPa, respectively, in a heat-treated sample, which retained the identical elongation of the as-printed specimen.

Keywords: additive manufacturing; nickel-based superalloy; solution and aging treatment; dislocations; precipitates; tensile properties

Citation: Ma, K.; Wang, J. Microstructural Characteristics and Mechanical Properties of an Additively Manufactured Nickel-Based Superalloy. *Crystals* **2022**, *12*, 1358. https://doi.org/10.3390/cryst12101358

Academic Editor: Lei Yang

Received: 29 August 2022
Accepted: 13 September 2022
Published: 26 September 2022

1. Introduction

Additive manufacturing (AM) processes, for instance, selective laser melting (SLM) and laser directed energy deposition (LDED) technologies, could directly produce complicated parts from three-dimensional designs without expensive tooling or forms (e.g., punches and dies) due to their manufacturing flexibility in metallic structural materials [1]. Over the decades, such techniques have been used to manufacture numerous alloys, such as Ti alloys, nickel-based superalloys, austenitic steels, martensitic steels, and Al alloys [2–7]. It was found that there were differences in microstructure and mechanical performances between the alloys processed by conventional and AM technologies [8–12]. In a recent study by Wang et al. [8], the austenitic 316 L stainless steels with both good yield stress and ductility were additively manufactured using a laser powder bed fusion process. The observed cellular structures, low-angle grain boundaries, and dislocations were found to enhance strength and the hierarchically heterogeneous microstructure, with length scales spanning nearly six orders of magnitude causing high uniform elongation. These distinctive cell structures containing numerous dislocations were also found in other alloys processed by AM, which was beneficial to their mechanical properties [10–12]. For instance, Liu et al. [10] found that both the strength and ductility of stainless steel could be improved by introducing the special dislocation network by SLM. Lee et al. [12] further proposed that the preferential precipitation along dislocation cell boundaries would deteriorate the resistance of hydrogen embrittlement in AM Inconel 718 alloy, which could be eliminated by suitable post heat treatments.

In past decades, a lot of attention was paid to the AM of nickel-based superalloys, which showed excellent high-temperature tensile strength, enhanced oxidation resistance, weldability, fatigue resistance, corrosion resistance, long-term structure stability, and were applied in the high-temperature parts of aeroengines and industrial gas turbines [3,12–15]. Previous studies showed that the high laser energy density and rapid cooling rate during AM processes resulted in a solidification substructure including Laves phases, as well as micro-segregation of alloy elements [3,15]. To improve mechanical properties, post heat treatments were also needed to form γ' (generally a face-centered cubic Ni_3Al with $L1_2$ structure) and γ'' precipitates (normally a body-centered tetragonal Ni_3Nb with $D0_{22}$ structure) as nickel-based superalloys processed by traditional techniques [15–18]. Zhang et al. [15] examined the influence of a standard heat treatment on the microstructure and mechanical performance of a SLM-manufactured superalloy. Further, Wang et al., [16] found that the SLM-fabricated Inconel 718 sample showed different creep performance and fracture behaviour from as-forged and as-cast samples, due to its unique microstructure. However, an in-depth understanding of the relationship between microstructure, mechanical properties, and the function of post heat treatment for AM nickel-based superalloys is still lacking [17–20].

In this work, a nickel-based superalloy was first manufactured by optimized SLM processes. Then the microstructural characteristics and mechanical performances of as-printed and heat-treated alloy specimens were systematically examined by optical microstructure (OM), electron backscattering diffraction (EBSD), transmission electron microscopy (TEM), and tensile testing. In Section 2, the experimental materials and methods are presented. In Section 3, the microstructural characteristics of as-printed and heat-treated samples are shown. Then, the tensile properties and fracture surfaces of as-printed and heat-treated nickel-based superalloy samples are given. The effect of heat treatment on the evolutions of microstructure and mechanical properties are discussed. Finally, the conclusions are summarized in Section 4.

2. Materials and Methods

In this study, nickel-based superalloy powders with an average size of 40 μm and the main chemical compositions shown in Table 1 were adopted. Then, alloy blocks with a size of 20 × 20 × 10 mm were printed using a commercial HBD-100D SLM machine (Guangdong Hanbang 3D Technology Co., Ltd., Zhongshan, China), as shown in Figure 1. During the SLM process, a range of various testing parameters were determined based on previous publications [3,12–23]. The selected parameters (listed in Table 2) were then tested by numerous orthogonal experiments based on density measurement and examination of defects (e.g., pores, internal cracks, un-melted areas, and spheroidization) using OM. The optimized processing parameters of layer thickness, hatch spacing, laser power, and scan speed were 30 μm, 0.11 mm, 175 W, and 825 mm/s, respectively. The density of the printed samples was about 8.17 g/cm^3, which was very close to the theoretical result of 8.19 g/cm^3.

Table 1. Main chemical compositions of the investigated nickel-based superalloy.

	Ni	Cr	Fe	Nb	Mo
Content (wt. %)	53.34	19.53	15.12	5.16	3.31

The printed alloy specimens were also subjected to a post heat treatment process of 1040 °C/1 h (solid solution treatment) and 700 °C/84 h (aging treatment), according to previous publications [13–16,19]. Both as-printed and heat-treated alloy specimens were machined for microstructural observation and mechanical testing. The OM microstructure was examined by an AXIOVERT40 metallography microscope. EBSD microstructure was obtained on a FEI QUANTA 200 SEM system after electrolytic polishing of the samples. The thin foil samples for TEM observation were electro-polished with 7% perchloric acid and a 93% methanol solution by double jets at −25 °C. The samples were then observed by a FEI Tecnai G2 F20 TEM system.

The flat, dog-bone-shaped tensile samples with gauge dimensions of $3 \times 8 \times 1.5$ mm^3 were machined by wire-electrode cuttings from the as-printed and heat-treated alloy blocks parallel to the building direction. To avoid residual stresses during the machining process, a double-stage machining process was used. First, a flat piece with a thickness of 1.5 mm was cut, then the tensile sample was cut from the flat piece. Tensile tests were then implemented on an INSTRON 3382 universal testing machine. The strain rate was 1×10^{-3} s^{-1}. The fractography was checked on a FEI QUANTA 200 SEM system.

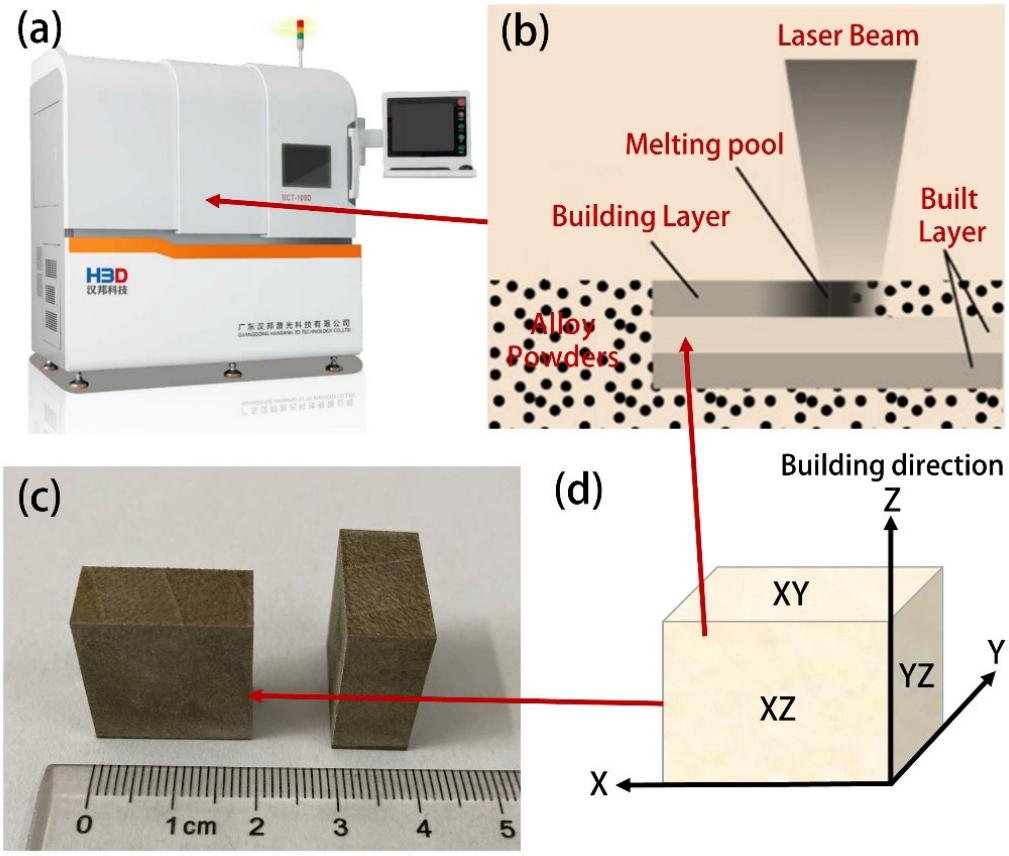

Figure 1. Illustrations of: (**a**) a commercial HBD-100D SLM machine, (**b**) SLM process, (**c**) as-printed samples, and (**d**) three-dimensional coordinated system of the investigated nickel-based superalloy specimen.

Table 2. Lists of testing parameters used to obtain the optimized processing parameters during SLM process.

	Layer Thickness (μm)	Hatch Spacing (mm)	Laser Power (W)	Scan Speed (mm/s)
Testing parameters	26, 28, 30, 32, 34, 36, 38, 40	0.5, 0.7, 0.9, 0.11, 0.13, 0.15	100, 125, 150, 175, 200, 225, 250	800, 825, 850, 875, 900

3. Results and Discussions

Figure 2 shows the OM and EBSD microstructures for different planes (as illustrated in Figure 1d) of the as-printed nickel-based superalloy sample. The OM of the XY plane (Figure 2a) showed a clear melting pool boundary with an elliptical trace and a certain orientation. The melting pool track is a long strip, whose orientation is the laser scanning path during printing. As shown in the figure, scanning directions between the layers were not the same, which was to reduce the anisotropy in the horizontal direction and residual stress. The width of the melting boundary was approximately 108.2 μm, which was roughly the same as the initial hatch spacing. On the other hand, the OMs of the YZ and XZ planes

(Figure 2c,e) presented arched melting pool morphology, owing to the function of the Gauss energy distribution of the laser beam and elongated dendrites within the melting pool [16–20]. To observe the corresponding dendrite structures of the as-printed sample, higher magnified EBSD metallographs were needed, as shown in Figure 2b,d,f. The EBSD microstructures of the as-printed alloy samples indicated typical columnar grains. In the XY plane, the grains appeared relatively equiaxed and evenly distributed, whereas in the YZ and XZ planes, we observed grain growth along the Z-axis.

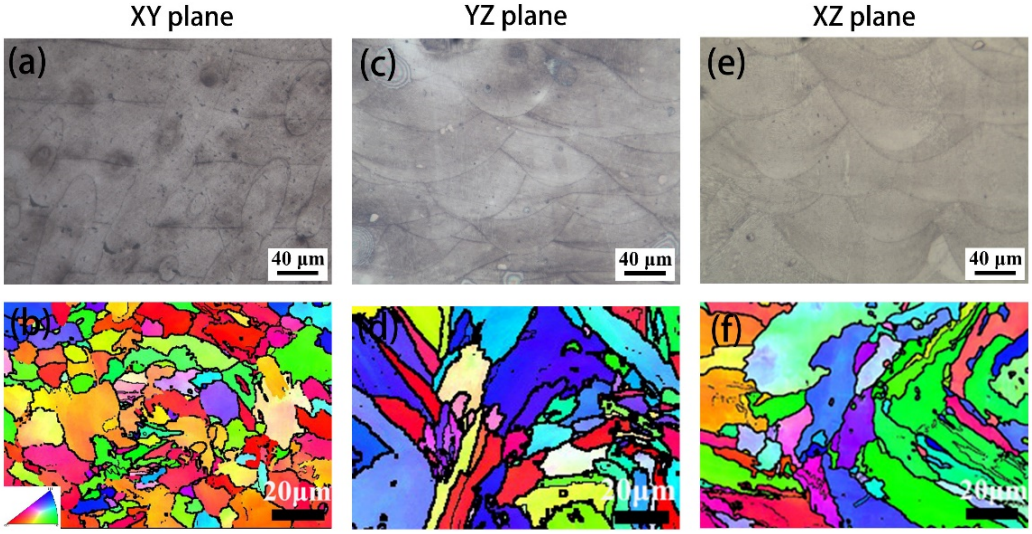

Figure 2. The OM and EBSD microstructures for different planes of the as-printed nickel-based superalloy specimen: (**a**) OM and (**b**) EBSD of XY plane, (**c**) OM and (**d**) EBSD of YZ plane, and (**e**) OM and (**f**) EBSD of XZ plane.

Figure 3 shows the OM and EBSD microstructures for the different planes following heat treatment. In all the observed planes, the melting pool traces almost disappeared in the OMs of the heat-treated specimen compared with the as-printed sample, which was also observed in previous studies [15,18,21]. Meanwhile, the grain boundaries were revealed by OM, which showed that a few finer grains and jagged grain boundaries were also observed. By comparing the EBSD microstructures in Figure 3b,d,f with those of Figure 2b,d,f, the initial grains in the as-printed sample (especially for primary grains with a larger size) were grown to some extent due to the partial recrystallization or grain growth that happened during the solid solution treatment [15,18,21]. As a result, fine and coarse grain zones interchanged in various planes, but the general grain size of heat-treated samples remained fine. In Table 3, we summarize the statistical results of grain size for the different planes in the as-printed and heat-treated nickel-based superalloys, based on EBSD observations. For the XY plane, the approximately equiaxial grains slightly grew from 9.02 to 11.85 μm, and mixed grains with coarse ones larger than 20 μm were observed. From the YZ and XZ planes, the primary grain profiles of the as-printed specimen grew epitaxially along the building direction, and the grain aspect ratio along the vertical section showed slight change after heat treatment. The overall grain size (length or width) also increased slightly. In addition, the coarsened grains after heat treatments showed straighter boundaries.

Figure 4 presents the pole figure (PF) and inverse pole figure (IPF) of as-printed and heat-treated nickel-based superalloy samples for the XY, YZ, and XZ planes, respectively. The grain orientations of both samples were uniform according to the PFs, and the differences in texture were not very clear. The <001> grain orientation of the XY plane were observed to be enhanced for all crystal planes after heat treatment. For YZ and XZ planes, the groups of (100) <001> grain orientation were strengthened, whereas the (110) <111> and (111) <101> grain orientations were weakened in heat-treated specimens. Such changes could be due to the observed recrystallization or grain growth in Figures 2 and 3.

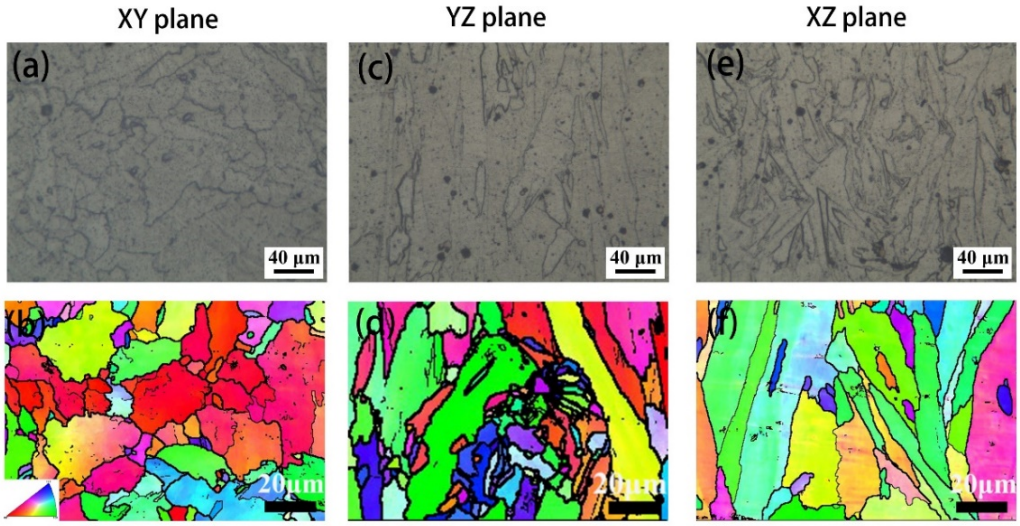

Figure 3. The OM and EBSD microstructures for different planes of the heat-treated nickel-based superalloy specimen: (**a**) OM and (**b**) EBSD of XY plane, (**c**) OM and (**d**) EBSD of YZ plane, and (**e**) OM and (**f**) EBSD of XZ plane.

Table 3. The statistical results of grain size in the as-printed and heat-treated nickel-based superalloy, based on EBSD observations (Unit: μm).

	As-Printed Sample			Heat-Treated Sample		
	Length (L) (μm)	**Width (W) (μm)**	**Ratio (L/W)**	**Length (L) (μm)**	**Width (W) (μm)**	**Ratio (L/W)**
XY plane	9.02		1	11.85		1
YZ plane	14.47	6.78	2.13	15.74	8.87	1.77
XZ plane	17.63	6.83	2.58	21.26	8.18	2.59

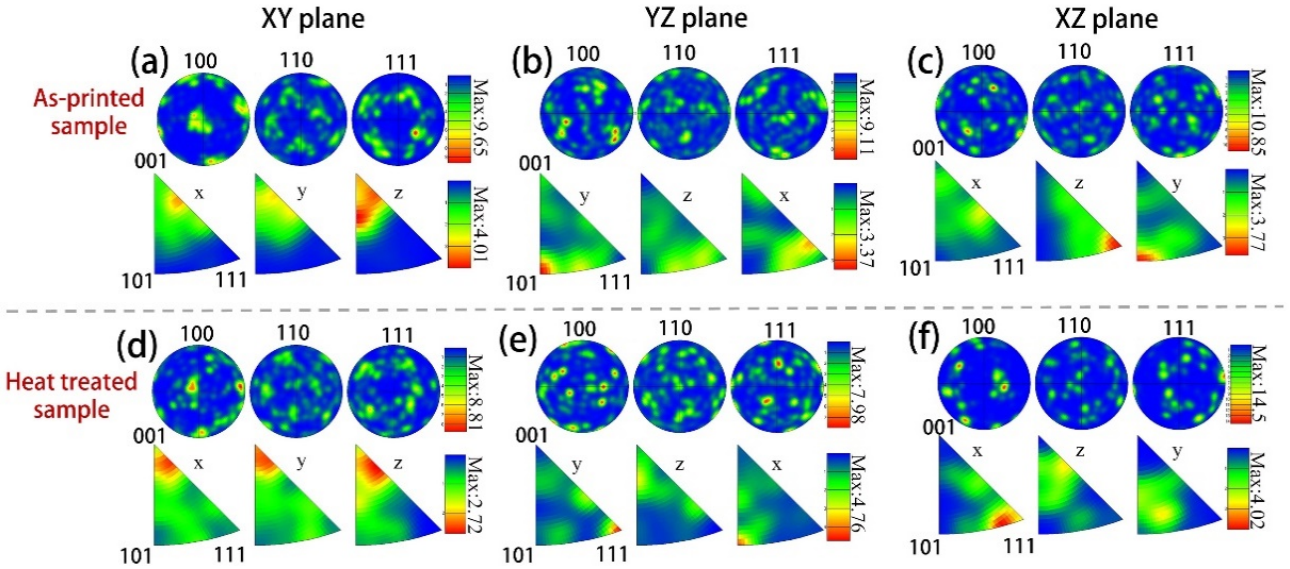

Figure 4. The pole figures (PFs) and inverse pole figures (IPFs) of (**a**–**c**) as-printed and (**d**–**f**) heat-treated nickel-based superalloy samples for XY, YZ, and XZ planes, respectively.

Figure 5 indicates the substructures and precipitates under TEM of the as-printed and heat-treated nickel-based superalloy specimens. In Figure 5a, a clear cellular microstructure with fine subgrains is observed in the as-printed nickel-based superalloy specimen. The primary grains (Figure 2) were fractionized into smaller regions by a network of sub-grain

boundaries. As a result, the substructure in adjacent grains showed little distinction in the orientation. The average size of cellular substructures was approximately 0.5 µm. To show greater detail, a high magnification image of cellular substructure is shown in Figure 5b. It is evident that the sub-grain boundaries are equivocal and contain discontinuous Laves phases and high density of dislocations. Furthermore, some entangled dislocations were also observed within the cellular substructure. Post heat treatment, as shown in Figure 5d, the subgrains grew to be about 0.8 µm with lower density of dislocations. The boundaries became straighter and the discontinuous Laves phases almost disappeared. Meanwhile, numerous nano-sized γ' and γ'' precipitates with length ~11 nm and width ~4 nm were formed, as shown in Figure 5c,e,f. The precipitates separated in two directions in an orthogonal distribution. According to the [001] selected area electron diffraction (SAED) patterns (Figure 5c), the precipitates were found to yield an orientation relationship of $(001)[100]\gamma'//(100)[001]\gamma$ or $(001)[100]\gamma''//(100)[001]\gamma$. In addition, the high-resolution TEM image in Figure 5e shows that the observed precipitate forms coherently, and its tetragonal distortion results in considerable coherency strains.

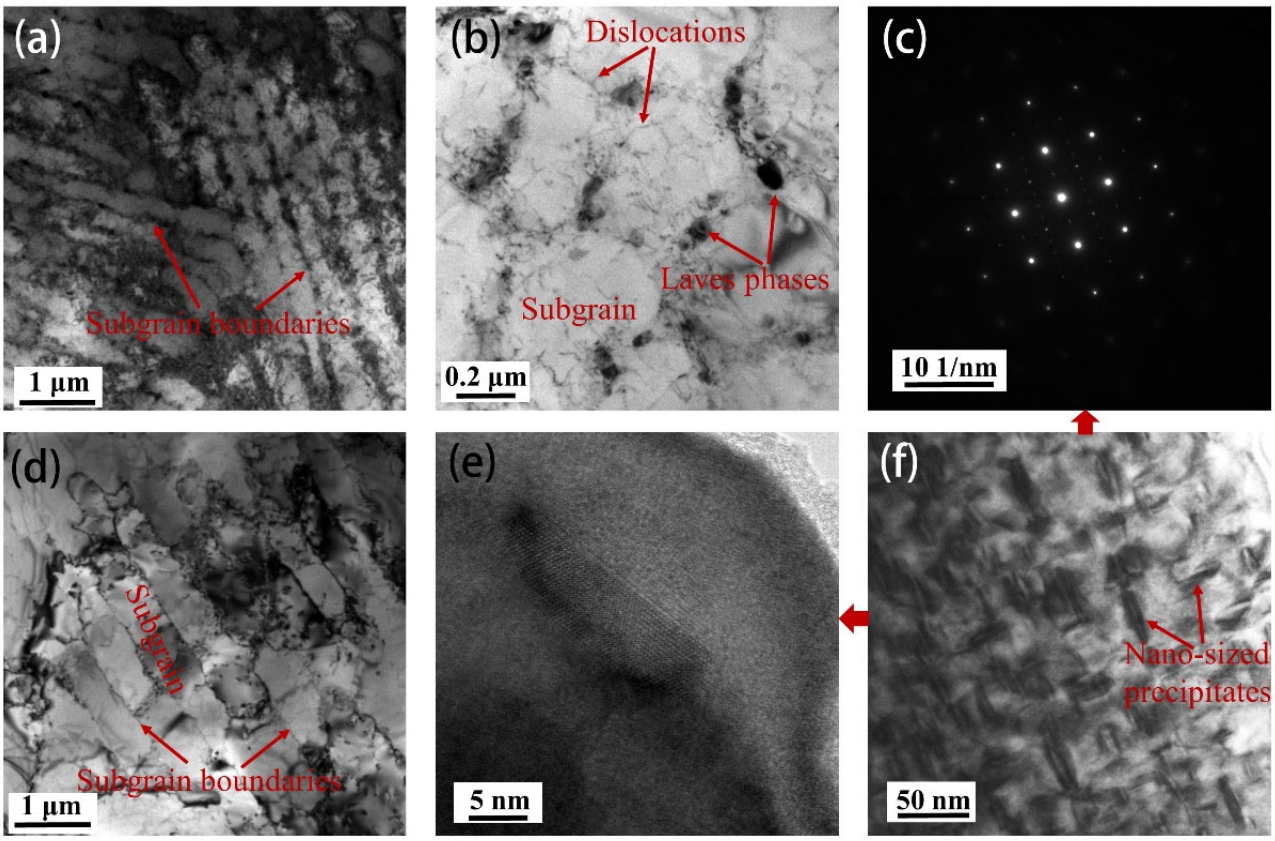

Figure 5. TEM images showing the substructures and precipitates of (**a**,**b**) as-printed and (**c**–**f**) heat-treated nickel-based superalloy samples.

In Figure 6a,b, the tensile properties of the as-printed and heat-treated alloy specimens are compared and summarized. The yield stress (σ_y) and tensile strength (σ_T) of the as-printed sample were 982 and 1181 MPa, respectively. After heat treatment, σ_y increased to 1362 MPa and σ_T increased to 1410 MPa, which was better than in previous studies [17–21]. Meanwhile, the elongations of the as-printed and heat-treated alloy specimens were almost identical. Hence, the applied heat treatment enhanced strength remarkably by retaining ductility. On the hand, the work hardening behavior of the as-printed sample was more notable than in the heat-treated specimen. In Figure 6c,d, the SEM fracture surfaces of the as-printed and heat-treated nickel-based superalloy specimens are given. Deep dimples were found in both alloy samples, which were distributed uniformly. The sizes of dimples

in heat-treated specimens were larger than those in the as-printed specimen, which may have been a result of different work hardening behaviors in Figure 6a [3,19].

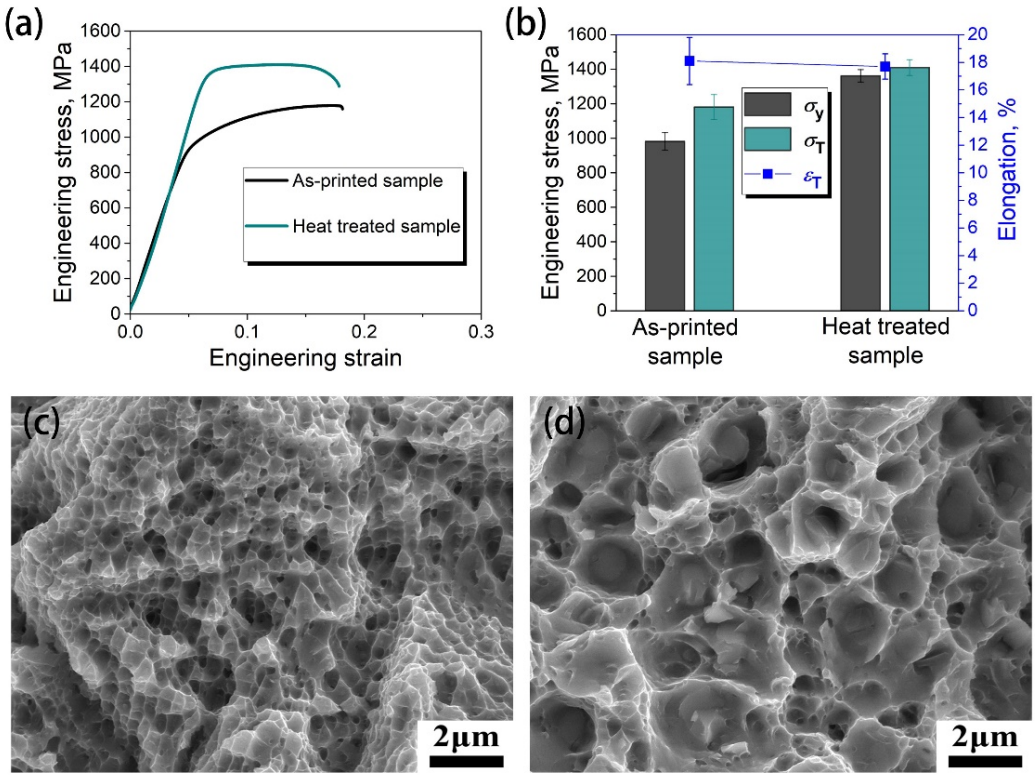

Figure 6. The (**a**,**b**) tensile properties and (**c**,**d**) SEM fracture surfaces of the as-printed and heat-treated nickel-based superalloy specimens.

It is known that the SLM process differs from classical manufacturing technologies. In general, the rapid solidification rate as well as high temperature gradient introduced during SLM could inhibit the formation of nano precipitates [20–23]. Furthermore, the size of the Laves phase was finer (Figure 5b) than that of traditional nickel-based superalloys, which made the Laves phase rapidly dissolve into the alloy matrix during post heat treatment (Figure 5d). On the other hand, the high solidification rate and steep temperature gradient during SLM processing could lead to numerous residual stresses. The repeated compression-tension cycles made by the regional thermal inhomogeneity, as well as the deviation of the thermal expansion coefficient between the Laves phase and alloy matrix were also identified. The high solidification rate prevented macrosegregation completely. These above factors lead to the formation of a high density of dislocations as well as fine subgrains, as shown in Figure 5a, which resulted in a high work hardening rate in the as-printed alloy sample (Figure 6a). For nickel-based superalloys, the Laves phase was pernicious to mechanical performances and led to Nb segregation, whereas the γ' and γ'' precipitates were major component of strengthening phases. Hence, the dissolution of the Laves phase during solution treatment would release Nb and form γ'/γ'' precipitates by annealing at lower temperatures, which are key to improving mechanical properties. Hence, in this study, the applied solution heat treatment was to dissolve Laves phase into the alloy matrix, and an aging process was carried out to precipitate fine γ' and γ'' phases with different sizes and shapes. Furthermore, the discontinuous Laves phases in Figure 5b could pin dislocations and subgrain boundaries. The serrated grain boundaries moved slowly and the grain only slightly grew during subsequent heat treatments. As a result, we gained remarkably improved yield stress and tensile strengths in the heat-treated alloy specimens. Further research is needed investigate the interrelation between the processes, structures, properties, and performances (e.g., fatigue, creep resistances, and mechanical

behaviours under dynamic loading and high temperature) of such additively manufactured nickel-based superalloys [1,19]. In addition, the in-situ heat treatment was also a promising approach to more efficient process of nickel-based superalloys [5].

4. Conclusions

We studied the microstructural characteristics and mechanical performances of an additively manufactured nickel-based superalloy. The key conclusions are summarized as follows:

(1) A nickel-based superalloy sample with good mechanical properties (σ_y = 982 MPa, σ_T = 1181 MPa, and ε_T = 18.2%) and few defects was manufactured by SLM. By performing post heat treatments, the σ_y and σ_T were further increased to 1362 and 1410 MPa, respectively, retaining the identical elongation of the as-printed specimen. Massive dimples were found in the fracture surfaces of both as-printed and heat-treated specimens.

(2) In the as-printed nickel-based superalloy sample, a fine grain size with uniform grain orientation was observed. After heat treatments, the grains only slightly grew. Meanwhile, the <001> grain orientation of the XY plane was observed to be enhanced for all crystal planes after heat treatment. For YZ and XZ planes, the groups of (100) <001> grain orientation were strengthened, whereas the (110) <111> and (111) <101> grain orientations were weakened in the heat-treated specimens.

(3) The special cellular substructure with a size of approximately 0.5 μm was found under TEM, where massive dislocations and discontinuous Laves phases were also observed in the as-printed specimen. After heat treatments, fine subgrains and fewer dislocations were retained. Further, massive nano-sized γ' and γ'' precipitates with the orientation relationship of $(001)[100]\gamma'//(100)[001]\gamma$ or $(001)[100]\gamma''//(100)[001]\gamma$ were formed to remarkably enhance the mechanical performances of the studied nickel-based superalloy.

Author Contributions: Conceptualization, K.M. and J.W.; methodology, K.M.; validation, K.M. and J.W.; data curation, K.M.; writing—original draft preparation, K.M. and J.W.; writing—review and editing, K.M. and J.W.; supervision, J.W.; project administration, J.W. All authors have read and agreed to the published version of the manuscript.

Funding: This research received no external funding.

Institutional Review Board Statement: Not applicable.

Informed Consent Statement: Not applicable.

Data Availability Statement: Not applicable.

Conflicts of Interest: The authors declare no conflict of interest.

References

1. DebRoy, T.; Wei, H.L.; Zuback, J.S.; Mukherjee, T.; Elmer, J.W.; Milewski, J.O.; Beese, A.M.; Wilson-Heid, A.; De, A.; Zhang, W. Additive manufacturing of metallic components—Process, structure and properties. *Prog. Mater. Sci.* **2018**, *92*, 112–224. [CrossRef]
2. Su, J.L.; Xie, H.M.; Tan, C.L.; Xu, Z.L.; Liu, J.; Jiang, F.L.; Tang, J.; Fu, D.F.; Zhang, H.; Teng, J. Microstructural characteristics and tribological behavior of an additively manufactured Ti-6Al-4V alloy under direct aging and solution-aging treatments. *Tribol. Int.* **2022**, *175*, 107763. [CrossRef]
3. Zhao, Y.N.; Ma, Z.Q.; Yu, L.M.; Dong, J.; Liu, Y.C. The simultaneous improvements of strength and ductility in additive manufactured Ni-based superalloy via controlling cellular subgrain microstructure. *J. Mater. Sci. Technol.* **2020**, *27*, 724–744. [CrossRef]
4. Xiao, J.; Lei, Y. Enriching Semantics of Geometry Features and Parameters for Additive Manufacturing Peculiar Structure Based on STEP Standards. *Crystals* **2022**, *12*, 1154. [CrossRef]
5. Herzog, D.; Seyda, V.; Wycisk, E.; Emmelmann, C. Additive manufacturing of metals. *Acta Mater.* **2016**, *117*, 371–392. [CrossRef]
6. Martin, J.H.; Yahata, B.D.; Hundley, J.M.; Mayer, J.A.; Schaedler, T.A.; Pollock, T.M. 3D printing of high-strength aluminium alloys. *Nature* **2017**, *549*, 365–369. [CrossRef]

7. Seede, R.; Shoukr, D.; Zhang, B.; Whitt, A.; Gibbons, S.; Flater, P.; Elwany, A.; Arroyave, R.; Karaman, I. An Ultra-High Strength Martensitic Steel Fabricated using Selective Laser Melting Additive Manufacturing: Densification, Microstructure, and Mechanical Properties. *Acta Mater.* **2020**, *186*, 199–214. [CrossRef]
8. Wang, Y.M.; Voisin, T.; McKeown, J.T.; Ye, J.C.; Calta, N.P.; Li, Z.; Zeng, Z.; Zhang, Y.; Chen, W.; Roehling, T.T.; et al. Additively manufactured hierarchical stainless steels with high strength and ductility. *Nat. Mater.* **2018**, *17*, 63–71. [CrossRef]
9. Bäker, M.; Rösler, J. Effect of Co and Cr on the Stability of Strengthening Phases in Nickelbase Superalloys. *Crystals* **2022**, *12*, 1084. [CrossRef]
10. Liu, L.F.; Ding, Q.Q.; Zhong, Y.; Zou, J.; Wu, J.; Chiu, Y.L.; Li, J.X.; Zhang, Z.; Yu, Q.; Shen, Z.J. Dislocation network in additive manufactured steel breaks strength–ductility trade-off. *Mater. Today* **2018**, *21*, 354–361. [CrossRef]
11. Fu, J.; Li, H.; Song, X.; Fu, M.W. Multi-scale defects in powder-based additively manufactured metals and alloys. *J. Matet. Sci. Technol.* **2022**, *122*, 165–199. [CrossRef]
12. Lee, D.H.; Zhao, Y.K.; Lee, S.Y.; Ponge, D.; Jägle, E.A. Hydrogen-assisted failure in Inconel 718 fabricated by laser powder bed fusion: The role of solidification substructure in the embrittlement. *Scr. Mater.* **2022**, *207*, 114308. [CrossRef]
13. Yuan, K.; Guo, W.; Li, D.; Li, P.; Zhang, Y.; Wang, P. Influence of heattreatments on plastic flow of laser deposited Inconel 718: Testing and microstructural based constitutive modeling. *Int. J. Plast.* **2021**, *136*, 102865. [CrossRef]
14. Maksimkin, I.P.; Yukhimchuk, A.A.; Malkov, I.L.; Boitsov, I.E.; Musyaev, R.K.; Buchirin, A.V.; Baluev, V.V.; Vertei, A.V.; Shevnin, E.V.; Shotin, S.V.; et al. Effect of Hydrogen on the Structure and Mechanical Properties of 316L Steel and Inconel 718 Alloy Processed by Selective Laser Melting. *Materials* **2022**, *15*, 4806. [CrossRef] [PubMed]
15. Zhang, D.Y.; Niu, W.; Cao, X.Y.; Liu, Z. Effect of standard heat treatment on the microstructure and mechanical properties of selective laser melting manufactured Inconel 718 superalloy. *Mater. Sci. Eng. A* **2015**, *644*, 32–40. [CrossRef]
16. Wang, L.Y.; Zhou, Z.J.; Li, C.P.; Chen, G.F.; Zhang, G.P. Comparative investigation of small punch creep resistance of Inconel 718 fabricated by selective laser melting. *Mater. Sci. Eng. A* **2019**, *745*, 31–33. [CrossRef]
17. Song, H.Y.; Lam, M.C.; Chen, Y.; Wu, S.; Hodgson, P.D.; Wu, X.H.; Zhu, Y.M.; Huang, A.J. Towards creep property improvement of selective laser melted ni-based superalloy in738lc. *J. Mater. Sci. Technol.* **2022**, *112*, 301–314. [CrossRef]
18. Hu, Y.L.; Lin, X.; Zhang, S.Y.; Jiang, Y.M.; Lu, X.F.; Yang, H.O.; Huang, W.D. Effect of solution heat treatment on the microstructure and mechanical properties of Inconel 625 superalloy fabricated by laser solid forming. *J. Alloy. Compd.* **2018**, *767*, 330–344. [CrossRef]
19. Shahwaz, M.; Nath, P.; Sen, I. A critical review on the microstructure and mechanical properties correlation of additively manufactured nickel-based superalloys. *J. Alloy. Compd.* **2022**, *907*, 164530. [CrossRef]
20. Wu, S.; Song, H.Y.; Peng, H.Z.; Hodgson, P.D.; Wang, H.; Wu, X.H.; Zhu, Y.M.; Lam, M.C.; Huang, A.J. A microstructure-based creep model for additively manufactured nickel-based superalloys. *Acta Mater.* **2022**, *224*, 117528. [CrossRef]
21. Huang, W.P.; Yang, J.J.; Yang, H.H.; Jing, G.Y.; Wang, Z.M.; Zeng, X.Y. Heat treatment of Inconel 718 produced by selective laser melting: Microstructure and mechanical properties. *Mater. Sci. Eng. A* **2019**, *750*, 98–107. [CrossRef]
22. Wang, S.; Tao, S.; Peng, H. Influence of Powder Characteristics on the Microstructure and Mechanical Behaviour of GH4099 Superalloy Fabricated by Electron Beam Melting. *Metals* **2022**, *12*, 1301. [CrossRef]
23. Savinykh, A.S.; Garkushin, G.V.; Razorenov, S.V.; Atroshenko, S.A.; Klimova-Korsmik, O.G.; Kislov, N.G. Strength Properties of the Heat-Resistant Inconel 718 Superalloy Additively Manufactured by Direct Laser Deposition Method under Shock Compression. *Metals* **2022**, *12*, 967. [CrossRef]